Surface & Coatings Technology 374 (2019) 1015–1023

Contents lists available at ScienceDirect

Surface & Coatings Technology

journal homepage: www.elsevier.com/locate/surfcoat

Corrosion behavior of ZnO-reinforced coating on aluminum alloy prepared by plasma electrolytic oxidation

Qian Huang[a], Zhongzhen Wu[a,b,c,*], Hao Wu[a], Shunping Ji[a], Zhengyong Ma[a], Zhongcan Wu[a], Pinghu Chen[a], Jiayu Zhu[a], Ricky K.Y. Fu[b,c], Hai Lin[a], Xiubo Tian[a], Feng Pan[a], Paul K. Chu[b,c]

[a] School of Advanced Materials, Peking University Shenzhen Graduate School, Shenzhen 518055, China
[b] Department of Physics, City University of Hong Kong, Tat Chee Avenue, Kowloon, Hong Kong, China
[c] Department of Materials Science and Engineering, City University of Hong Kong, Tat Chee Avenue, Kowloon, Hong Kong, China

ARTICLE INFO

Keywords:
Al alloys
Zinc oxide
Plasma electrolytic oxidation
Corrosion resistance

ABSTRACT

Aluminum alloys are widely used in the aerospace and transportation industries, but the corrosion resistance is insufficient in long-term service especially in the high salinity environment. A ceramic coating composed of ZnO nanoparticles is demonstrated to significantly improve the corrosion resistance of the Al alloys. Owing to the similar chemical activity of Zn and Al, ZnO particles fuse into Al_2O_3 in the micro-arc during plasma electrolytic oxidation (PEO) rendering the coating compactness. The formation mechanism of the PEO coating is investigated and discussed. The corrosion current of the ZnO modified PEO coating is 4 orders of magnitude less than that of the LY12 substrate. Immersion tests performed in 3.5 wt% sodium chloride show that incorporation of ZnO prevents destruction and dissolution of the PEO coating in the high salinity environment.

1. Introduction

Aluminum alloys are used widely in the automotive and aerospace industry because of desirable physical properties such as the low density, high strength, good casting ability, and low cost [1,2]. However, the relatively high chemical reactivity of Al and Al alloys leads to easy corrosion under harsh conditions in spite of the native surface passivation film [3,4]. Plasma electrolytic oxidation (PEO), which can produce a thick, hard, and adherent ceramic alumina-based coating on aluminum alloys [5], is an effective technique to improve the corrosion resistance [6,7]. Nevertheless, pores and defects are inevitably formed during PEO because of the drastic discharge-cooling and gas evolution processes, which produce porous coating that lack the barrier ability against corrosion especially in harsh environments [8,9].

Generally, sealing the pores of PEO coating can increase the corrosion resistance. Different methods have been utilized to minimize the size and number of pores in PEO coating. For example, post-treatment in boiling water can decrease the pore size of PEO coating, but it is still difficult to completely fill the pores to improve the corrosion resistance [10]. Some organic materials such as benzotriazole, poly(L-lactide) (PLLA), and others can be applied to seal the pores [11,12] and significant enhancement is obtained because of the inertness of organic materials. However, organic materials have poor thermal stability and aging resistance, resulting in insufficient durability. Recently, some inert inorganic particles with nanometer to micrometer size have been proposed to seal pores by adding the particles into the electrolyte during PEO [13,14]. For example, incorporation of SiO_2 nano-particles decreases the surface roughness and reduces the corrosion current density about 8 times compared to 7075 Al alloys [15] and CeO_2 particles added in PEO coatings decrease the corrosion current density about 9 times compared titanium alloy substrate [16]. In addition, the incorporation of CuO, TiO_2, and Al_2O_3 have also been found to bring some beneficial effects [17–19]. However, corroding droplets can still penetrate the coating in long-time service as shown by salt spraying and it may be attributed to aggregation of particles and most of particles being isolated in the Al_2O_3 matrix [20].

Owing to the large band gap, small conductivity and similar chemical inertness as alumina [21–23], ZnO has been widely used as filler materials to improve the corrosion resistance of some organic materials [24,25]. Furthermore, the reducibility of Zn is slightly smaller than that of Al [26,27] so that Al can capture O in ZnO at a high arc temperature resulting in fusion of ZnO and Al_2O_3 to form a compact composite coating [28]. In this work, ZnO nanoparticles are incorporated into PEO coating on Al alloys and the fusion behavior of the two oxides as well as corrosion resistance in a high salinity environment are assessed.

* Corresponding author at: School of Advanced Materials, Peking University Shenzhen Graduate School, Shenzhen 518055, China.
E-mail address: wuzz@pku.edu.cn (Z. Wu).

https://doi.org/10.1016/j.surfcoat.2019.06.079
Received 7 April 2019; Received in revised form 29 May 2019; Accepted 26 June 2019
Available online 28 June 2019

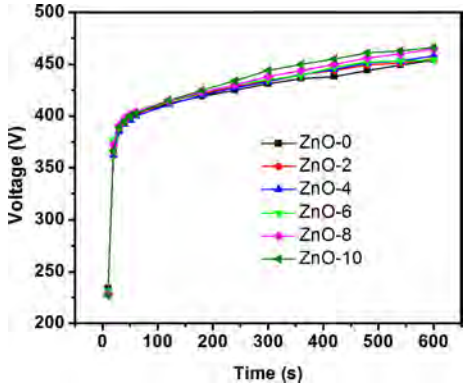

Fig. 1. Anodic voltage vs. treatment time during the PEO process in the constant current mode.

2. Experimental details

2.1. Sample preparation

The commercial polished LY12 Al alloy was used as the substrate in PEO. Before PEO, the substrate was cut into plates (25 × 50 × 2 mm) and cleaned ultrasonically in acetone and ethanol for 10 min. The deionized aqueous solution containing sodium silicate (Na_2SiO_3, 15 g/L) and sodium hexametaphosphate ($(NaPO_3)_6$, 10 g/L) was used as the electrolyte. ZnO particles (300–500 nm, Aladdin Inc., China) with concentrations varying from 0 to 10 g/L were added to the electrolyte and the samples were labeled as ZnO-0, ZnO-2, ZnO-4, ZnO-6, ZnO-8, and ZnO-10, respectively, where the number represented the concentration of zinc oxide in the electrolyte. PEO was performed on a custom system comprising a DC pulsed power supply (Plasma Technology Ltd., Hong Kong) and stainless steel solution container serving as the cathode. The process was conducted at a constant positive current density of 5 A∗dm^{-2}, frequency of 100 Hz, and duty cycle of 30% for 10 min. During PEO, the temperature of the electrolyte was controlled to be below 55 °C with a mechanical stirrer.

2.2. Materials characterization

The surface morphology was examined by field-emission scanning electron microscopy (FE-SEM, Carl Zeiss, SUPRA® 55, Germany) and the surface and lateral elemental distributions were determined by energy-dispersive X-ray spectroscopy (EDS). The microstructure was further examined by high-resolution transmission electron microscopy (HR-TEM, FEI, Technai F20, USA). The composition of samples was characterized by grazing incidence X-ray diraction (GIXRD, Rigaku Smartlab, Japan) with Cu K_α radiation ($\lambda = 0.15418$ nm) at an incidence angle of 1°. The XRD data were collected in the 2θ range of 10°–80° using a step size of 0.01° and a scanning rate of 5°/min.

2.3. Corrosion evaluation

The corrosion characteristics of the aluminum alloy substrate and PEO samples was monitored in a sodium chloride solution (NaCl, 3.5 wt %). The electrochemical measurements were carried out on the CHI 660E electrochemical workstation based on the three-electrode system with the potential referenced to the saturated calomel electrode (SCE) and platinum sheet counter electrode. The potentiodynamic test was conducted with the coated sample being the working electrode, saturated calomel electrode (SCE) as the reference electrode, and platinum rod ($\varphi = 20$ mm) as the counter electrode. The specimen with a surface area of 2.5 cm^2 was exposed to NaCl solution. After 10 min to stabilize the open-circuit potential (OCP), the potentiodynamic polarization tests were conducted from −0.25 V to 0.5 V (vs. SCE) at a scanning rate of 1 mV/s. After stabilization for 10 min, the electrochemical impedance spectra (EIS) were collected to investigate the electrode/solution interface. The data were recorded from 100 kHz to 100 mHz with a 5 mV sinusoidal perturbing signal at the open-circuit potential. The potential was scanned from the cathodic to the anodic regions at a rate of 1 mV/s

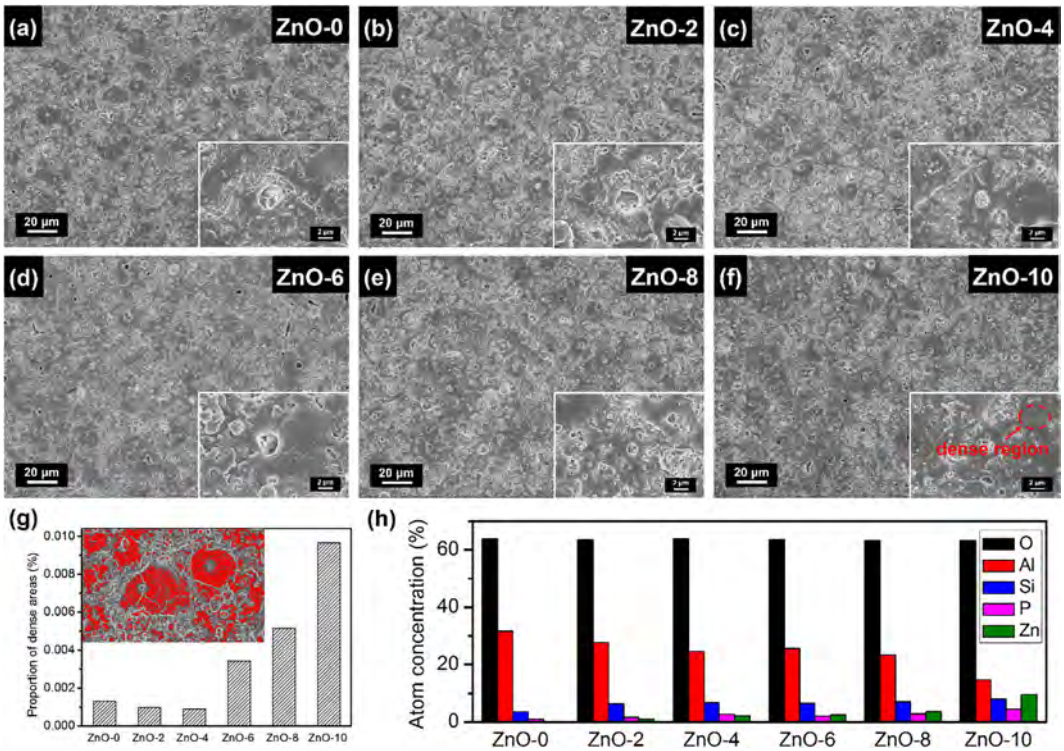

Fig. 2. (a)–(f) SEM micrographs showing the surface morphology for the PEO coating obtained in electrolytes containing different concentrations of ZnO particles; (g) Proportion of dense areas in the SEM images of the PEO samples; (h) Compositions of PEO coating determined by EDS.

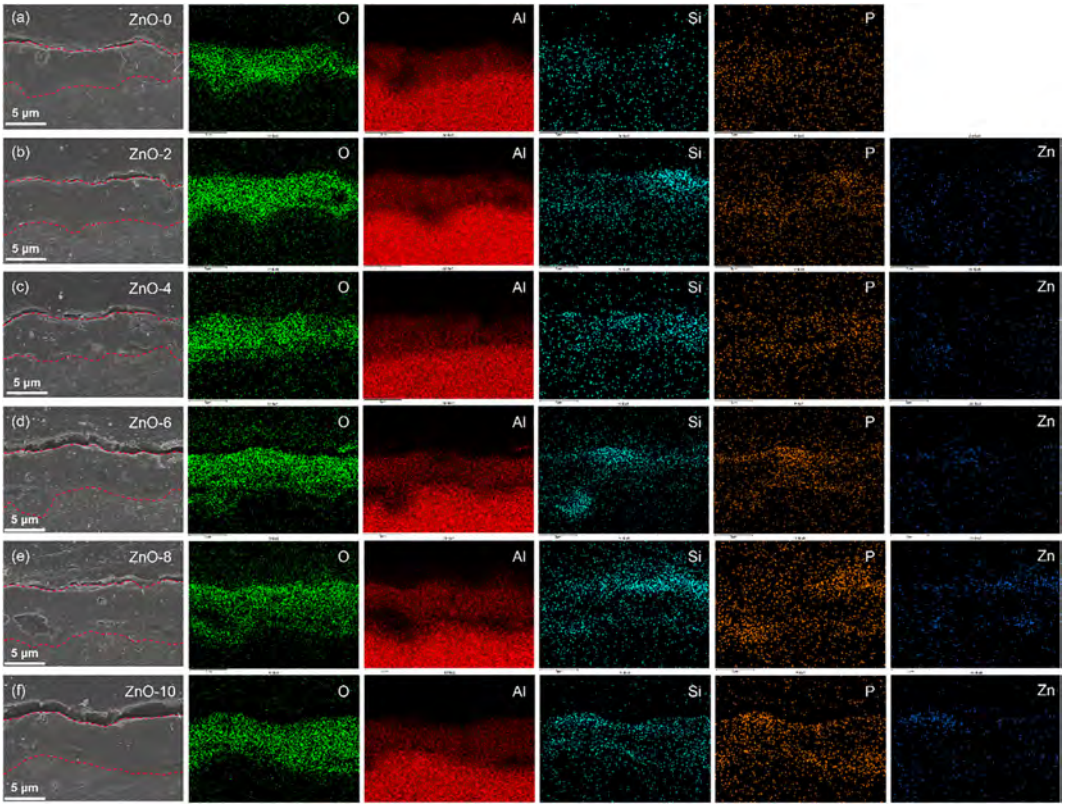

Fig. 3. SEM micrographs showing the cross-sections of the PEO films and EDS maps of the corresponding areas.

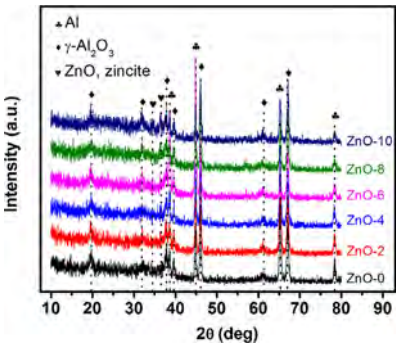

Fig. 4. Grazing incidence X-ray diffraction (GIXRD) spectra of the PEO coating obtained in electrolytes containing different concentrations of ZnO particles.

to acquire the polarization curves. Immersion tests were carried out to probe the corrosion behavior of the samples. After immersion in 3.5 wt % NaCl at room temperature for 2, 7, and 14 days, the samples were taken out, rinsed with water and ethanol, and dried in air. The surface morphology of corroded samples was observed by FE-SEM and confocal laser scanning microscopy (CLSM, VK-X200, KEYENCE, Japan) and the elemental composition was determined by EDS.

3. Result and discussion

Fig. 1 shows the voltage evolution during PEO at a constant current density. The working voltage increases rapidly to about 380 V in the initial 20 s indicating rapid electrochemical formation of the initial oxide film [29]. The voltage increases slower afterward and sparks moving over the entire sample surface are observed due to breakdown of the oxide layer and generation of micro-discharges [30]. The voltage increases gradually reaching a plateau of 400 V to 450 V. The overall trend of the V-T curves is not affected significantly by the addition of

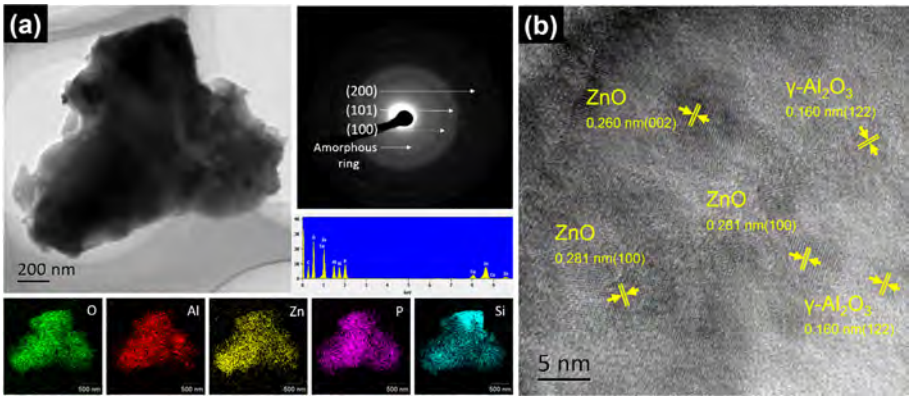

Fig. 5. (a) Low-resolution TEM micrograph of a fragment from the ZnO-10 PEO film with the inset at the top-right corner showing the SAED pattern of the related area, inset at the right-middle position showing the EDS spectrum of the related area, and insets on the bottom showing the EDS maps of different elements; (b) High-resolution TEM micrograph taken from area (a).

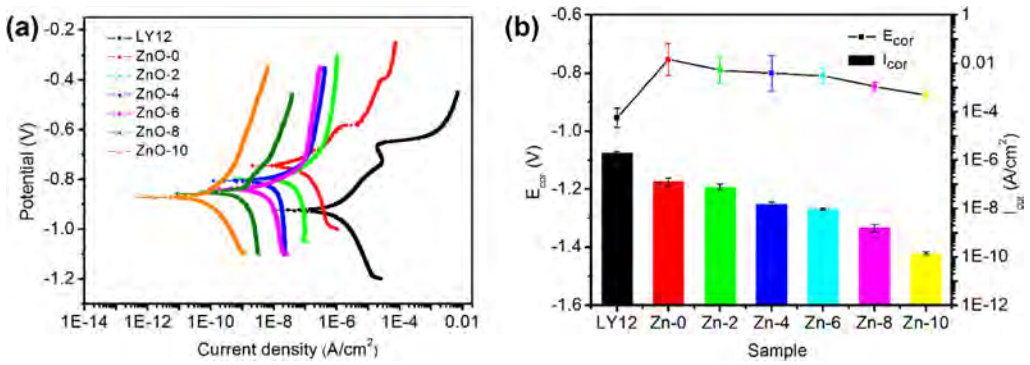

Fig. 6. (a) Potentiodynamic polarization curves of the untreated and PEO-treated LY12 alloy samples after immersion in 3.5 wt% NaCl solution for 600 s; (b) Comparison of the corrosion potential (E_{cor}) and corrosion current density (I_{cor}) values calculated from the polarization curves.

Table 1
E_{cor}, I_{cor}, and β_c of different samples in 3.5 wt% NaCl calculated from the polarization curves.

	E_{cor} (V vs. SCE)	I_{cor} (A∗cm^{-2})	β_c (V/decade)
LY12	−0.954 ± 0.034	(1.93 ± 0.30) × 10^{-6}	0.309 ± 0.017
ZnO-0	−0.753 ± 0.055	(1.37 ± 0.48) × 10^{-7}	0.548 ± 0.051
ZnO-2	−0.79 ± 0.046	(8.03 ± 2.27) × 10^{-8}	0.994 ± 0.187
ZnO-4	−0.80 ± 0.061	(1.57 ± 0.29) × 10^{-8}	0.819 ± 0.016
ZnO-6	−0.81 ± 0.026	(9.65 ± 0.91) × 10^{-9}	0.786 ± 0.025
ZnO-8	−0.846 ± 0.015	(1.65 ± 0.59) × 10^{-9}	0.689 ± 0.062
ZnO-10	−0.876 ± 0.011	(1.42 ± 0.21) × 10^{-10}	0.255 ± 0.012

ZnO particles but the working voltage increases slightly with ZnO concentration in the electrolyte.

The surface morphology for the PEO coating is shown in Fig. 2. All the samples have the typical rough and porous microstructure. As the concentration of zinc oxide increases, the pores become smaller and shallower because of the sealing by ZnO particles. The proportion of dense areas derived from the SEM images indicates that the coating become denser after incorporation of ZnO particles as shown in Fig. 2(g). Fig. 2(h) shows that the ZnO-incorporated PEO coating consists of O, Al, Si, and P and Zn. The atomic concentrations of Zn are 0.92%, 2.13%, 2.48%, 3.67%, and 5.07% corresponding to PEO coating formed in 2, 4, 6, 8, and 10 g/L ZnO electrolytes, respectively. As the Zn concentration goes up, both Si and P increase but Al decreases in the PEO coating, indicating that phosphate and silicate can be taken into the ZnO-doped PEO coating.

Fig. 3 displays the cross-sectional SEM images and corresponding EDS maps of the PEO samples. All the samples possess a dense and compact PEO but a wavy interface between the coating and substrate is observed. The thickness of the coating increases with the addition of ZnO particles. Zn is mainly enriched in the outer porous layer of the coating and Si and P become more concentrated as the concentration of ZnO increases.

The GIXRD patterns of the PEO coating and untreated Al alloy are depicted in Fig. 4. The typical Al diffraction peaks from the aluminum substrate are observed and there is a broad peak between 2θ of 20°–35° indicative of amorphous phases. It has been reported that the amorphous phases formed in PEO in a silicate electrolyte are mainly alumina and silica [25] and in the $(NaPO_3)_6$ electrolyte, $AlPO_4$ is formed [26]. Besides, the diffraction peaks at 19.5°, 31.9°, 37.7°, 39.5°, 45.9°, 60.9°,

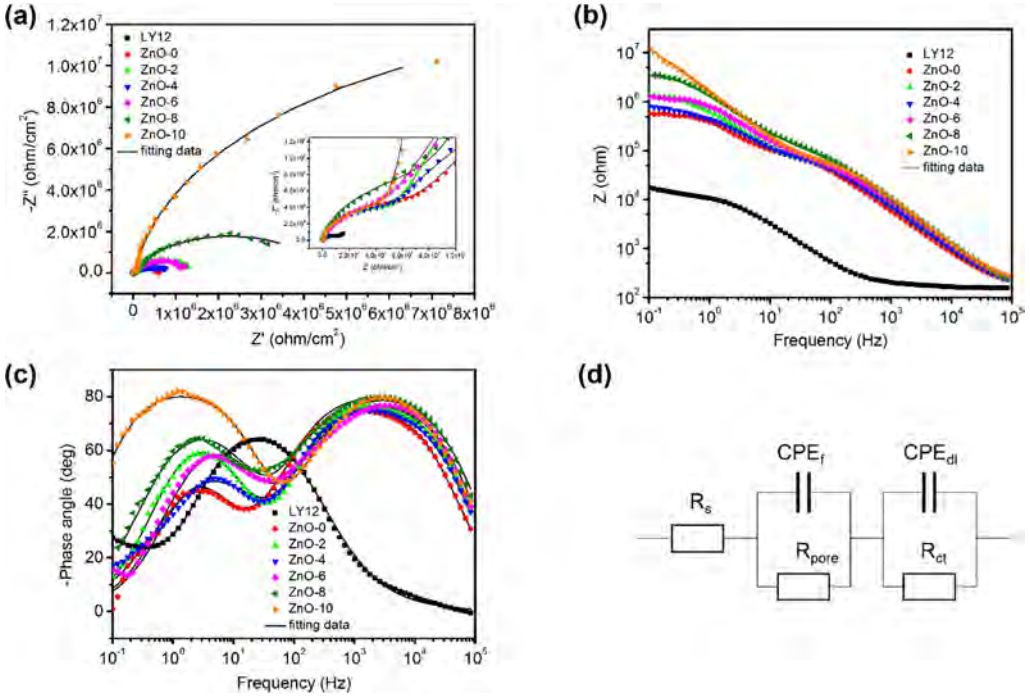

Fig. 7. (a) Nyquist plots; (b) Bode impedance plots; and (c) Bode phase angle plots of the untreated and PEO-treated LY12 alloy samples after immersion in 3.5 wt% NaCl solution for 600 s; (d) Equivalent circuit for the fitted EIS data.

Table 2
Fitted EIS results for different samples in 3.5 wt% NaCl based on the corresponding equivalent circuit models.

	LY12	ZnO-0	ZnO-2	ZnO-4	ZnO-6	ZnO-8	ZnO-10
R_s (ohm∗cm^{-2})	160.6 ± 0.95	177 ± 4.10	171.3 ± 2.56	149.7 ± 4.99	161.1 ± 5.84	151.6 ± 5.12	201.1 ± 3.51
Y_f (ohm^{-2}∗cm^{-2}∗S^{-n})	(8.62 ± 0.186) ∗ 10^{-6}	(8.636 ± 0.291) ∗ 10^{-8}	(5.26 ± 1.225) ∗ 10^{-8}	(5.102 ± 0.4067) ∗ 10^{-8}	(5.435 ± 0.3215) ∗ 10^{-8}	(3.859 ± 0.2201) ∗ 10^{-8}	(3.382 ± 0.0996) ∗ 10^{-8}
n_f	0.906 ± 0.0072	0.8834 ± 0.0045	0.9137 ± 0.0028	0.9591 ± 0.0129	0.9077 ± 0.0081	0.9446 ± 0.0089	0.9343 ± 0.0031
R_{pore} (ohm∗cm^{-2})	9394 ± 249.2	(7.311 ± 0.285) ∗ 10^4	(5.655 ± 0.1043) ∗ 10^4	(4.091 ± 0.2036) ∗ 10^4	(4.845 ± 0.2745) ∗ 10^4	(7.524 ± 0.4025) ∗ 10^4	(5 ± 0.087) ∗ 10^4
Y_{dl} (ohm^{-2}∗cm^{-2}∗S^{-n})	(1.23 ± 0.063) ∗ 10^{-4}	(4.43 ± 0.137) ∗ 10^{-7}	(2.745 ± 0.0357) ∗ 10^{-7}	(4.308 ± 0.0841) ∗ 10^{-7}	(1.943 ± 0.0593) ∗ 10^{-7}	(1.405 ± 0.0287) ∗ 10^{-7}	(1.125 ± 0.0088) ∗ 10^{-7}
n_{dl}	0.6195 ± 0.0074	0.8982 ± 0.0148	0.8931 ± 0.5051	0.7701 ± 0.0079	0.8704 ± 0.0109	0.8659 ± 0.0084	0.9448 ± 0.0028
R_{ct} (ohm∗cm^{-2})	(8.27 ± 3.027) ∗ 10^4	(5.453 ± 0.118) ∗ 10^5	(1.375 ± 0.0148) ∗ 10^6	(8.325 ± 0.1422) ∗ 10^5	(1.301 ± 0.0255)∗10^6	(4.378 ± 0.1093) ∗ 10^6	(2.557 ± 0.0835) ∗ 10^7
χ^2	$4.605 * 10^{-4}$	$1.38 * 10^{-3}$	$4.608 * 10^{-4}$	$1.019 * 10^{-3}$	$1.866 * 10^{-3}$	$1.437 * 10^{-3}$	$6.079 * 10^{-4}$

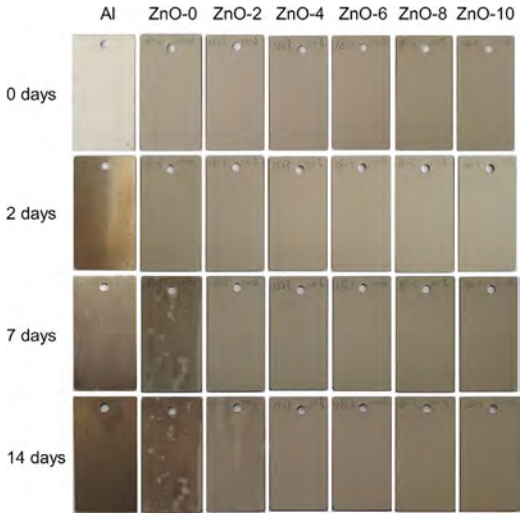

Fig. 8. Snapshots taken after immersion for different time from the untreated and PEO-treated LY12 alloy samples in 3.5 wt% NaCl solution.

and 67° are associated with γ-Al_2O_3 (JCPDS NO. 10-0425) and those at 34.4° and 36.3° stem from ZnO (Zincite, JSPDS NO. 36-1451) in the ZnO-incorporated samples providing more evidence of the existence of ZnO in the coating.

The ZnO-10 sample was further investigated by transmission electron microscopy (TEM). Fig. 5(a) shows the low-resolution TEM image of a fragment from the ZnO-incorporated PEO coating. The EDX mapping result shows that all elements such as Al, P, Si, O, and Zn are observed in the fragment of film. The SAED pattern in Fig. 5(a) shows an amorphous ring, as well as several crystalline rings that correspond to the face-centered cubic ZnO phase with random orientations. The high-resolution TEM image of the coating shows lattice fringes of ZnO (100), ZnO (002), and γ-Al_2O_3 (112), suggesting that a multiphase mixture of ZnO and γ-Al_2O_3 are formed. No obvious interface can be observed between the ZnO grains and alumina indicating effective fusion [2]. The fusion mechanism of ZnO in alumina at the high arcing temperature may be that the zinc oxide particles melt partially in the molten Al leaving behind small ZnO nanocrystals, or the ZnO particles melt completely and recrystallize during cooling after arcing [31].

Fig. 6(a) presents the potentiodynamic polarization (POL) curves of the aluminum alloy substrate and PEO samples in 3.5 wt% NaCl. The tests are conducted after immersion for 600 s to stabilize the open-circuit potential (OCP). The corrosion potential (E_{cor}) and corrosion current density (I_{cor}) are derived directly from the Tafel region in the cathodic polarization curves by Tafel extrapolation and the calculated E_{cor} and I_{cor} are listed in Table 1 and shown in Fig. 6(b). After PEO, the polarization curves shift to the positive side of the potential and smaller current density suggesting better corrosion resistance. After addition of ZnO, the corrosion current density decreases continuously from 8.03×10^{-8} A∗cm^{-2} to 1.27×10^{-10} A∗cm^{-2}, while the corrosion potential increases slightly from −0.79 V to −0.876 V. The improvement in the corrosion performance of the ZnO-incorporated samples can be contributed to the intrinsically inertness of ZnO [22,23] and the densification of the fusion with Al_2O_3. ZnO-10 exhibits the smallest corrosion current density which is about 800 times less than that of ZnO-0 sample and 4 orders of magnitude less than that of the LY12 substrate, which is much better than that of conventional doping without fusion [15,16].

The electrochemical impedance spectroscopy (EIS) results are shown in Fig. 7. The conductive loops of the Nyquist plots are enlarged after PEO indicating improved corrosion resistance. The PEO samples also show larger impedance modulus than the substrate, suggesting better corrosion protection performance [32,33]. The EIS data are simulated with an equivalent circuit and constant phase elements (CPE)

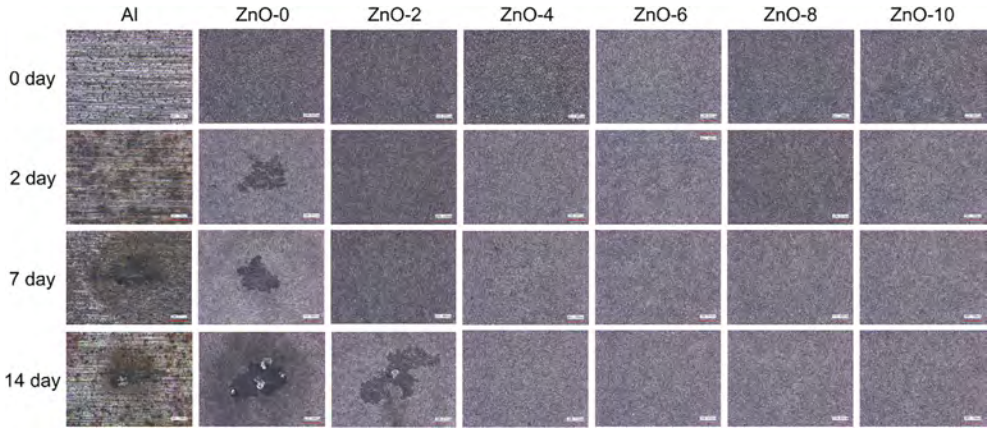

Fig. 9. Confocal laser scanning microscopy (CLSM) images taken after immersion for different times from the untreated and PEO-treated LY12 alloy samples in 3.5 wt % NaCl solution.

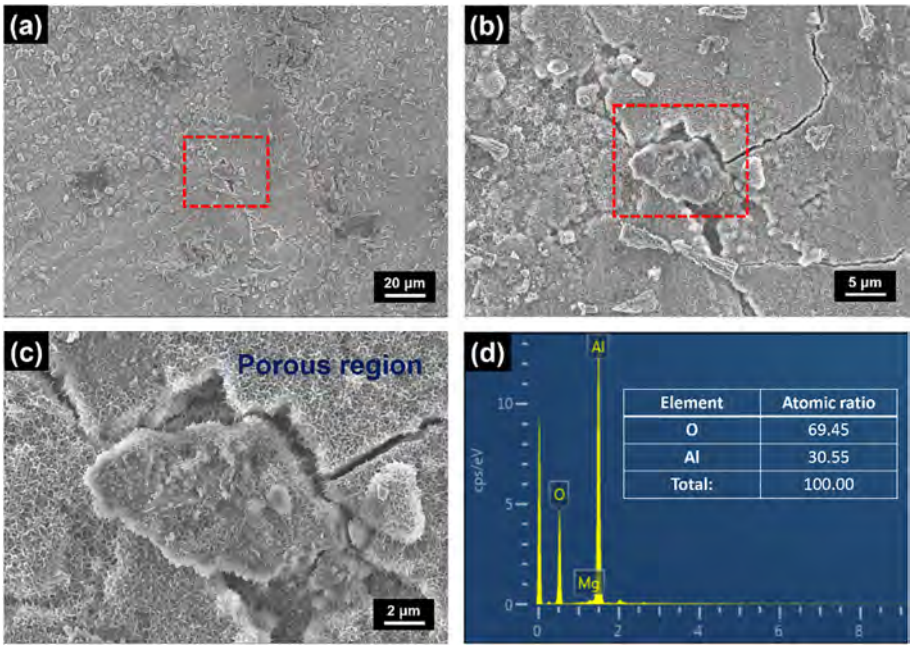

Fig. 10. (a) SEM image of a typical area on the LY12 sample after immersion in 3.5 wt% NaCl for 14 days; (b) and (c) Magnified region step-by-step; (d) Corresponding EDS results of area (c).

are used to represent the non-ideal capacitors as follows:

$$Y = Y_0 (j\omega)^n, \tag{1}$$

where Y_0 and n are the admittance constant and empirical exponent, respectively. Generally, the capacitive arc at high frequencies results from film effects and charge transfer, whereas that at low frequencies stems from mass transfer [34–37]. Here, $R_s(CPE_f(R_{pore}(CPE_{dl}R_{ct})))$ is used to simulate the EIS data. In the circuit, R_s stands for the solution resistance, CPE_f is the capacitance of the deposited or passivating film on the surface, R_{pore} is the sum of the resistance of the pores in the film, CPE_{dl} is the capacitance of the electric double layer, R_{ct} represents the related charge transfer resistance in the faradic process. From the fitting results shown in Table 2, the R_{ct} increases from $8.27 \times 10^4\ \Omega{\cdot}cm^2$ of LY12 to $5.453 \times 10^5\ \Omega{\cdot}cm^2$ of the ZnO-0 sample and $2.557 \times 10^7\ \Omega{\cdot}cm^2$ of the ZnO-10 sample, suggesting that the PEO coating effectively protects the substrate and the addition of ZnO further improves the corrosion resistance of the PEO coating [38,39].

Fig. 8 shows the images of different samples after continuous immersion in 3.5 wt% NaCl solution for 2, 7, and 14 days. The pristine PEO samples show a uniform grey surface and the samples with high ZnO concentrations are darker than those with low ZnO concentrations and ZnO-0. After immersion for 2 days, LY12 turns from a metallic luster to dark brown with localized pits, whereas the PEO samples show no corrosion pits. After 7 days, macroscopic corrosion is observed from ZnO-0 but the ZnO-incorporated samples show no corrosion. After 14 days, localized corrosion can be observed from ZnO-2 but the coating with larger ZnO concentrations remain intact, indicating that ZnO improves the corrosion resistance of the PEO coating and the corrosion resistance depends on the ZnO concentration. CLSM is performed to observe micro-corrosion of the samples after immersion. As shown in Fig. 9, localized pits start to emerge on both LY12 and ZnO-0 after 2 days and ZnO-2 after 14 days being consistent with the aforementioned images.

The surface morphology and corrosion behavior of the samples after immersion in 3.5 wt% NaCl for 14 days are displayed in Figs. 10–13. The LY12 substrate shows the typical corrosion characteristics of Al alloys manifested by a surface full of cracks and exfoliated fragments of the corrosion products as shown in Fig. 10. The corrosion cracks are attributed to stress released from the native passivation film as a result of corrosion product formation in the substrate [1]. ZnO-0 after

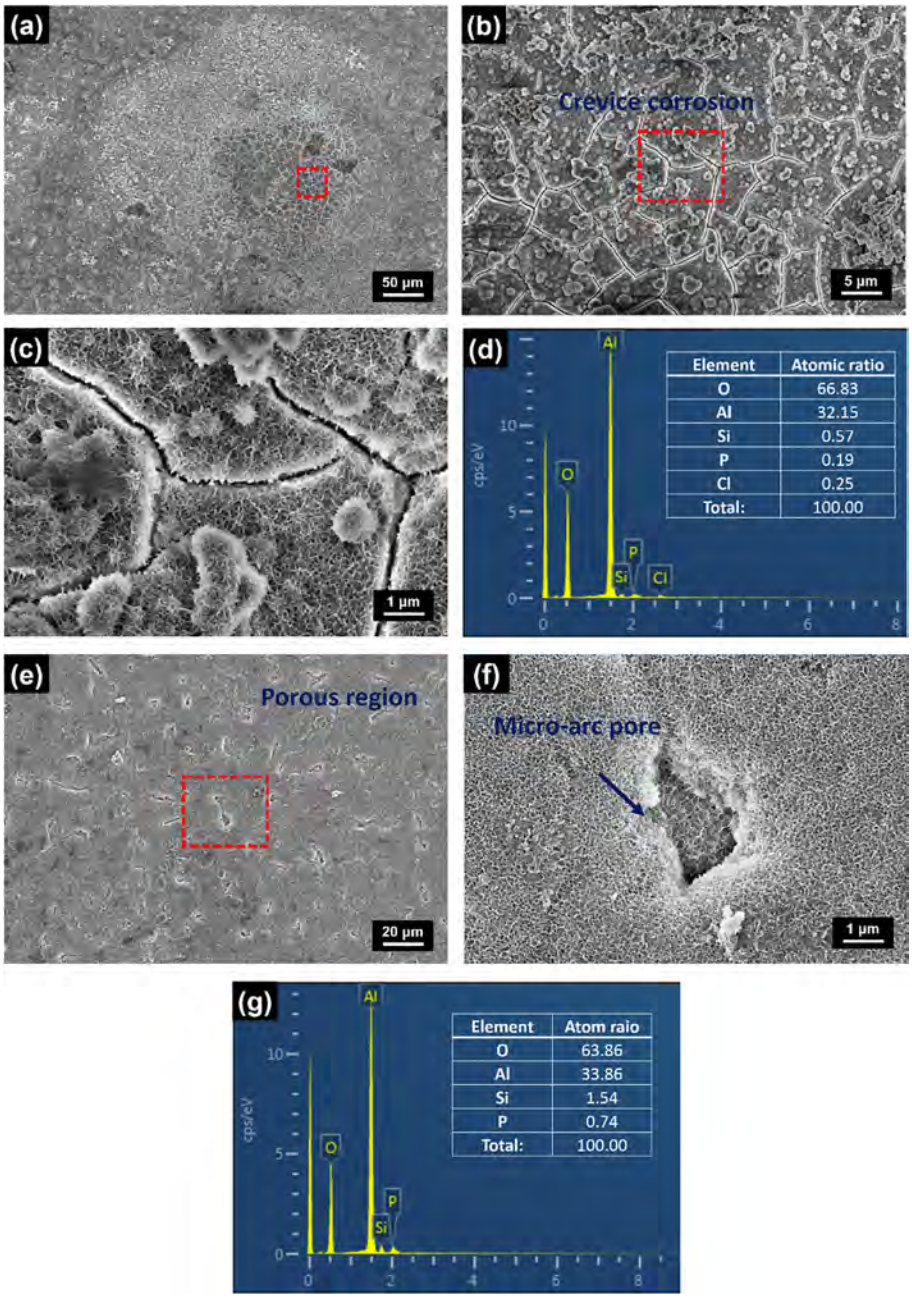

Fig. 11. (a) SEM image of a typical area on the ZnO-0 sample with crevice formation after immersion in 3.5 wt% NaCl for 14 days; (b) and (c) Magnified region step-by-step; (d) Corresponding EDS results of area (c); (e) SEM image of a non-crevice area on the ZnO-0 sample after immersion for 14 days; (f) Magnified view of the area; (g) Corresponding EDS results of area (f).

immersion for 14 days shown in Fig. 11 shows two different corrosion features. One has obvious crevice and bud-like corrosion products on the sample surface like the LY12 substrate (Fig. 11a–d). Generally, crevice formation in PEO coating results from volume expansion during formation of the corrosion products and additional stress caused by hydrogen bubble evolution [40], meaning that the corrosion droplets penetrate the PEO coating giving rise to severe corrosion of the substrate. The second one has no crevice at all (Fig. 11e–g) representing the typical PEO morphology comprising micro-arc pores and bud-like protrusions. A sponge-like structure can be observed from the surface and particularly the pores after immersion because of the different corrosion resistance of the multi-phase structure of the coating [41] confirmed by EDS.

Crevice corrosion can be observed from ZnO-2 after immersion for 14 days as shown in Fig. 12(a). However, different from the ZnO-0 sample, parts of the crevice region in ZnO-2 do not show a porous structure. EDS result shows that the crevice region contains O, Al, Si, P, and Zn and the P/Al ratio and Si/Al ratio are much higher than the ZnO-0 sample. This result suggests that the destruction of coating and the dissolution of P and Si component are inhibited by the incorporated ZnO. For the non-crevice region, a porous structure similar to the ZnO-0 sample covers on the most of the surface area. In the non-crevice regions, except for the porous structure, some non-porous areas are also observed from the surface. As shown in Fig. 12(f), non-porous area and typical areas of porous are marked as area A and area B, respectively. EDS results reveal that the area A containing Zn displays higher Si/Al and P/Al ratios comparing to the area B without ZnO. The SEM and EDS results suggest that the area containing ZnO keeps a higher content of Si and P and a more compact surface morphology. However, owing to the small concentration of ZnO, ZnO-2 is not protected adequately. Fig. 13

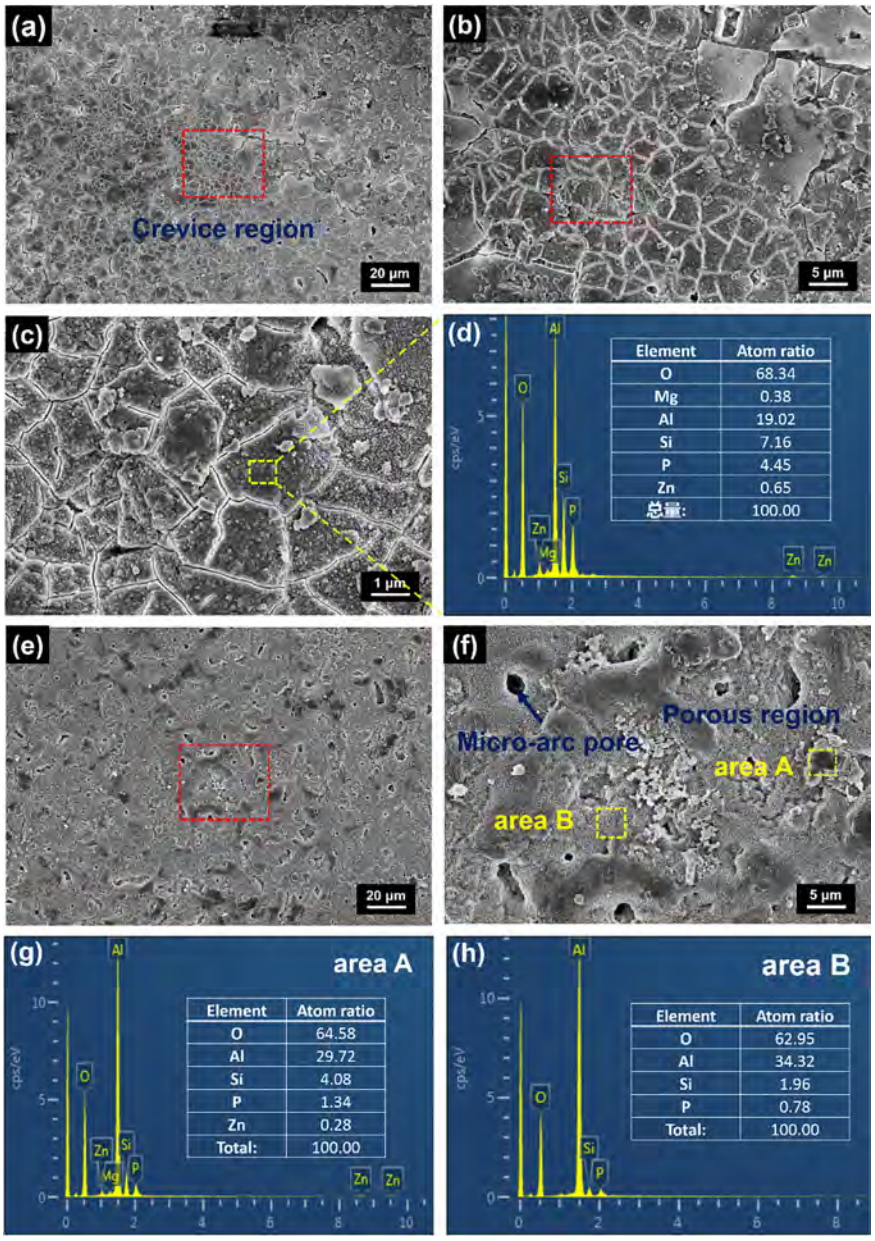

Fig. 12. (a) SEM image of a typical area on the ZnO-2 sample with crevice formation after immersion in 3.5 wt% NaCl for 14 days; (b) and (c) Magnified region step-by-step; (d) Corresponding EDS results of the selected area in (c); (e) SEM image showing a non-crevice area on the ZnO-2 sample after immersion for 14 days; (f) Magnified view of the area; (g)–(h) Corresponding EDS results of areas A and B in panel (f).

shows the surface morphology of ZnO-10 after immersion for 14 days. The surface has the typical surface morphology of a PEO film without crevices and porous feature. EDS reveals that the concentrations of Al, P, and Zn are similar to those before immersion implying that the composition barely changes and nearly no corrosion takes place during immersion.

4. Conclusion

The corrosion resistance of the LY12 Al alloy is improved by performing plasma electrolytic oxidation in the phosphate-silicate electrolyte containing ZnO particles. The ZnO particles incorporated into the PEO coating can fuse with alumina to form much denser PEO coating. Electrochemical tests show that the ZnO-incorporated PEO coating have improved corrosion resistance compared to the substrate or conventional a PEO coating without ZnO. The incorporated ZnO can protect the coating from corrosion in the NaCl solution.

Declaration of Competing Interest

None.

Acknowledgments

This work was financially supported by Soft Science Research Project of Guangdong Province (No. 2017B030301013), New Energy Materials Genome Preparation & Test Key-Laboratory Project of Shenzhen (No. ZDSYS201707281026184), Shenzhen Science and Technology Research Grants (JCYJ20170306165240649 , JCYJ20170818150601930), and Hong Kong Innovation and Technology Fund (ITF) ITS/452/17FP (CityU 9440179).

Author contributions

The authors made equal contributions.

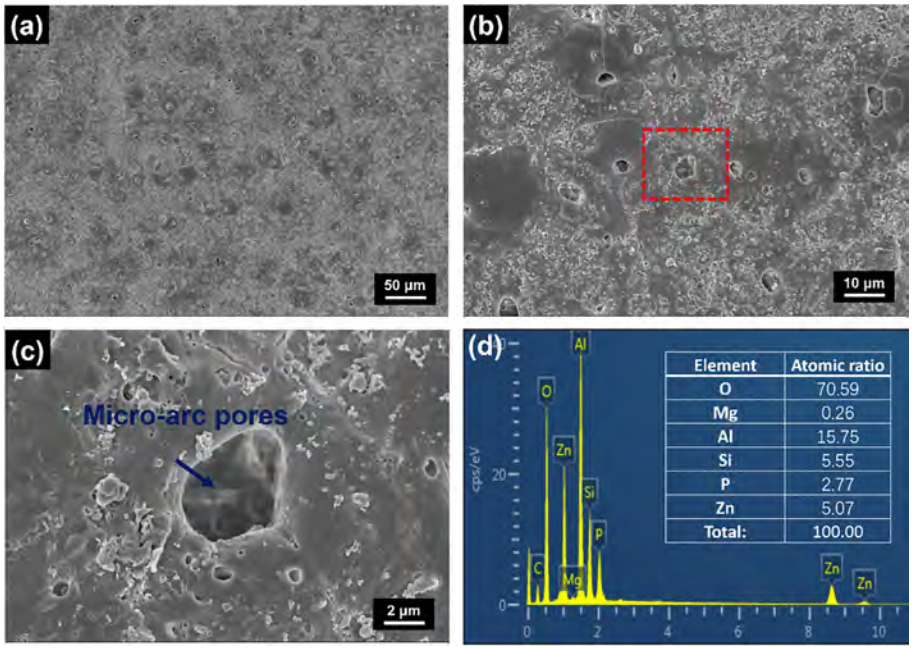

Fig. 13. (a) SEM image of a typical area on the surface of ZnO-10 sample after immersion in 3.5 wt% NaCl for 14 days; (b) and (c) Magnified region step-by-step; (d) Corresponding EDS results of area (c).

References

[1] W. Lei, Y. Wang, Z. Yu, J.H. Ouyang, L. Guo, D. Jia, Corros. Sci. 52 (2010) 2687–2696.
[2] R.-Q. Wang, Y.-K. Wu, G.-R. Wu, D. Chen, D.-L. He, D. Li, C. Guo, Y. Zhou, D. Shen, P. Nash, J. Alloys Compd. 753 (2018) 272–281.
[3] Q. Chen, Z. Jiang, S. Tang, W. Dong, Q. Tong, W. Li, Appl. Surf. Sci. 423 (2017) 939–950.
[4] U. Tiringer, J. Kovač, I. Milošev, Corros. Sci. 119 (2017) 46–69.
[5] A.L. Yerokhin, X. Nie, A. Leyland, A. Matthews, S.J. Dowey, Surf. Coat. Technol. 122 (1999) 73–93.
[6] S. Moon, Y. Jeong, Corros. Sci. 51 (2009) 1506–1512.
[7] L. Zhu, Z. Guo, Y. Zhang, Z. Li, M. Sui, Electrochim. Acta 208 (2016) 296–303.
[8] M.M. Krishtal, P.V. Ivashin, I.S. Yasnikov, A.V. Polunin, Met. Sci. Heat Treat. 57 (2015) 428–435.
[9] J. Zhao, X. Xie, C. Zhang, Corros. Sci. 114 (2017) 146–155.
[10] C. Chu, X. Han, F. Xue, J. Bai, P. Chu, Appl. Surf. Sci. 271 (2013) 271–275.
[11] M. Sun, A. Yerokhin, M.Y. Bychkova, D.V. Shtansky, E.A. Levashov, A. Matthews, Corros. Sci. 111 (2016) 753–769.
[12] Alyaa Alabbasi, Afrin Mehjabeen, M. Bobby Kannan, Qingsong Ye, Carsten Blawert, Appl. Surf. Sci. 301 (2014) 463–467.
[13] X. Lu, C. Blawert, K.U. Kainer, M.L. Zheludkevich, Electrochim. Acta 196 (2016) 680–691.
[14] X. Lu, M. Mohedano, C. Blawert, E. Matykina, R. Arrabal, K.U. Kainer, M.L. Zheludkevich, Surf. Coat. Technol. 307 (2016) 1165–1182.
[15] A. Bahramian, K. Raeissi, A. Hakimizad, Appl. Surf. Sci. 351 (2015) 13–26.
[16] S. Di, Y. Guo, H. Lv, J. Yu, Z. Li, Ceram. Int. 41 (2015) 6178–6186.
[17] H.-X. Li, R.-G. Song, Zh.-G. Ji, Trans. Nonferrous Metals Soc. China 23 (2013) 406–411.
[18] D. Kim, D. Sung, J. Lee, Y. Kim, W. Chung, Appl. Surf. Sci. 357 (2015) 1396–1402.
[19] W. Yan, D. Wei, Y. Jie, S. Di, J. Mater. Sci. Technol. 30 (2014) 984–990.
[20] A. Pardo, S. Merino, M.C. Merino, I. Barroso, M. Mohedano, R. Arrabal, F. Viejo, Corros. Sci. 51 (2009) 841–849.
[21] K. Han, M. Xie, L. Zhang, L. Yan, J. Wei, G. Ji, Q. Luo, J. Lin, Y. Hao, C.-Q. Ma, Sol. Energy Mater. Sol. Cells 185 (2018) 399–405.
[22] G. Kartopu, D. Turkay, C. Ozcan, W. Hadibrata, P. Aurang, S. Yerci, H.E. Unalan, V. Barrioz, Y. Qu, L. Bowen, A.K. Gürlek, P. Maiello, R. Turan, S.J.C. Irvine, Sol. Energy Mater. Sol. Cells 176 (2018) 100–108.
[23] Y. Ko, Y. Kim, S.Y. Kong, S.C. Kunnan, Y. Jun, Sol. Energy Mater. Sol. Cells 183 (2018) 157–163.
[24] S. Shen, Y. Zuo, Corros. Sci. 87 (2014) 167–178.
[25] B. Ramezanzadeh, M.M. Attar, Prog. Org. Coat. 71 (2011) 314–328.
[26] S.J. Pearton, D.P. Norton, K. Ip, Y.W. Heo, T. Steiner, Superlattices Microstruct. 34 (2005) 3–32.
[27] O. Madelung, U. Rössler, M. Schulz, Zinc oxide (ZnO) Debye temperature, heat capacity, density, melting point, vapor pressure, hardness, 41B (1999) 1–5.
[28] V.R. Kumar, P.R.S. Wariar, J. Koshy, J. Adv. Microsc. Res. 6 (2011) 306–312.
[29] R.O. Hussein, X. Nie, D.O. Northwood, Electrochim. Acta 112 (2013) 111–119.
[30] Z. Yao, Y. Jiang, F. Jia, Z. Jiang, F. Wang, Appl. Surf. Sci. 254 (2008) 4084–4091.
[31] X. Lu, C. Blawert, Y. Huang, H. Ovri, M.L. Zheludkevich, K.U. Kainer, Electrochim. Acta 187 (2016) 20–33.
[32] T.S. Lim, H.S. Ryu, S.-H. Hong, Corros. Sci. 62 (2012) 104–111.
[33] H. Wu, Z. Shi, X. Zhang, A.M. Qasim, S. Xiao, F. Zhang, Z. Wu, G. Wu, K. Ding, P.K. Chu, Appl. Surf. Sci. 478 (2019) 150–161.
[34] G. Song, A. Atrens, D.S. John, X. Wu, J. Nairn, Corros. Sci. 39 (1997) 1981–2004.
[35] Y. Zhang, C. Yan, F. Wang, W. Li, Corros. Sci. 47 (2005) 2816–2831.
[36] Y. Xin, T. Hu, P.K. Chu, Corros. Sci. 53 (2011) 1522–1528.
[37] H. Wu, S. Xiao, D. Chen, A.M. Qasim, K. Ding, G. Wu, P.K. Chu, Surf. Coat. Technol. 306 (2016) 6–10.
[38] Q. Zong, L. Wang, W. Sun, G. Liu, Corros. Sci. 89 (2014) 127–136.
[39] L.-Y. Cui, S.-D. Gao, P.-P. Li, R.-C. Zeng, F. Zhang, S.-Q. Li, E.-H. Han, Corros. Sci. 118 (2017) 84–95.
[40] Z.-Y. Ding, L.-Y. Cui, X.-B. Chen, R.-C. Zeng, S.-K. Guan, S.-Q. Li, F. Zhang, Y.-H. Zou, Q.-Y. Liu, J. Alloys Compd. 764 (2018) 250–260.
[41] S. Rahimi, A.B. Khiabani, B. Yarmand, A. Kolahi, Mater. Today Proc. 5 (2018) 15667–15676.